J. Fluid Mech. (2001), *vol.* 431, *pp.* 407–426. Printed in the United Kingdom

Stability of axially symmetric flow driven by a rotating magnetic field in a cylindrical cavity

By I. GRANTS AND G. GERBETH†

Forschungszentrum Rossendorf, Postfach 510119, 01314 Dresden, Germany

(Received 21 December 1999 and in revised form 29 September 2000)

This paper deals with the stability analysis of an axially symmetric liquid metal flow driven by a rotating magnetic field in a cylinder of finite dimensions. The limit of linear stability with respect to axially symmetric perturbations is found for diameter-to-height ratios between 0.4 and 1. This oscillatory instability is shown to be different from the expected Taylor–Görtler vortices. Several linearly unstable steady solutions are found close to the stable basic state. It is shown that small finite-amplitude perturbations in the form of Taylor–Görtler vortices give rise to instability in the linearly stable regime.

1. Introduction

An example of a rotating magnetic field (RMF) is the field generated in an induction motor. Obviously, a conducting liquid immersed in such a field follows the field rotation. Besides the primary azimuthal rotation, a secondary meridional flow is generated by the imbalance of the centrifugal force and the radial pressure gradient near the horizontal walls (Davidson 1992).

The stability of the flow driven by a rotating magnetic field in an infinite cylinder with no meridional recirculation was considered by Richardson (1974). The critical forcing parameter for the onset of the Taylor–Görtler type instability was obtained. The stability of the RMF-driven flow in a finite length cylinder is particularly important for various applications in semiconductor crystal growth techniques. The rotating magnetic field was proposed as a tool to eliminate the practically unavoidable thermal asymmetry and to control the heat and dopant transfer in such processes (Gelfgat *et al.* 1992). In this context the stability threshold marks the upper limit of the control possibilities since an oscillating flow causes inhomogeneity of the crystal grown (Hurle 1994). Therefore, this stability question has received wide interest in the crystal growth and magnetohydrodynamic applications community.

Different numerical simulations, e.g. by Gelfgat, Priede & Sorkin (1991), Kaiser & Benz (1998), Marty *et al.* (1999), Barz *et al.* (1997), Mößner & Gerbeth (1999), have shown that for aspect ratios around unity the near-critical basic flow is marked by a strong meridional recirculation and an almost rigidly rotating core, separated from the rigid walls by thin boundary layers. The vertical side layer of such a flow is considerably thiner than in the infinite cylinder case considered by Richardson (1974). Therefore it is not surprising that the Taylor–Görtler type instability sets in at a considerably stronger forcing than follows from Richardsons' analysis. However,

† Author to whom correspondence should be addressed: e-mail: gerbeth@fz-rossendorf.de

different numerical simulations failed to reproduce quantitative results that agreed even in the leading digit. Hence, the questions arise: What is behind such big discrepancies; and what is the actual stability limit? The objective of our investigation is to answer these questions.

The previous investigations, referred to numerical integration of the time-dependent solution and the critical parameter was determined as the limit when oscillatory solutions were obtained. Since these methods did not reproduce reliable results a more accurate and correct approach is needed. We approximate the solution by a set of functions constructed from orthogonal Chebyshev polynomials. The steady solution is found and the spectrum of the linearized problem is evaluated numerically for a continuously increasing forcing parameter.

The main result of the linear stability analysis is that the critical perturbation does not represent the Taylor–Görtler vortex instability reported before. However, our investigation reveals that there are unstable states very close to the linearly stable basic flow corresponding to a small-amplitude perturbation in the form of Taylor–Görtler vortices. The estimated minimum amplitude of such an unstable finite perturbation shows that the experimental observation of a linear instability would require a very high accuracy.

Section 2 introduces the mathematical problem. Numerical techniques are briefly described in § 3. Section 4 contains the main results, which are discussed in § 5. The conclusions are given in § 6.

2. Formulation of the problem

The axially symmetric flow of an electrically conducting incompressible Newtonian fluid with kinematic viscosity ν, electrical conductivity σ in a cylinder of radius R_0 and height $2H_0$ is considered. The flow is driven by a uniform magnetic field of induction B_0 rotating in a plane $z = \text{const}$ with a constant angular frequency ω. The induced magnetic body force has an axially symmetric mean part and a three-dimensional part oscillating with double frequency 2ω. The effect of the oscillating force part has recently been investigated by Martin Witkowski & Walker (1999). Our model of the magnetic force considers low-frequency and low-induction conditions, hence taking into account only the time-averaged part. The low-frequency approximation requires a skin depth much larger than the radius of the cylinder $(\omega\sigma\mu)^{-1/2} \gg R_0$, where μ is the magnetic permeability of the fluid. The low-induction condition implies that the flow does not influence the driving magnetic body force. This is fulfilled by $\omega \gg \Omega_0$ (Moffatt 1965), where Ω_0 is the characteristic angular velocity of the resulting flow. This condition can be expressed in terms of the field characteristics (Priede 1993): $Ha^2 \ll Re_\omega^{1/2}$, where $Ha = (\sigma/(2\rho\nu))^{1/2} B_0 H_0$ is the Hartmann number and $Re_\omega = \omega H_0^2/\nu$ is a Reynolds number corresponding to the field rotation. We assume $Ha^2 \ll 1$ in our investigation, for which the condition above is satisfied if $Re_\omega > 1$. Once the low-induction condition is satisfied the axial symmetry follows from the estimate $u'/u \propto \Omega_0/\omega$ derived by Davidson & Hunt (1987). Here u'/u denotes the relative amplitude of three-dimensional oscillations due to the oscillating part of the driving force.

An analytical solution can be written for the averaged magnetic body force under these conditions (Gorbachev, Nikitin & Ustinov 1974). It has only an azimuthal component, which can be presented in the form $F_\phi = 0.5\sigma\omega B_0^2 r\, f(z,r)$, where the shape function $f(z,r)$ reflects the influence of the finite length of the cylinder. The

shape function

$$f(z,r) = 1 - \frac{R_0}{r}\sum_{k=1}^{\infty}\frac{2J_1(\lambda_k r/R_0)}{(\lambda_k^2-1)J_1(\lambda_k)}\frac{\cosh(\lambda_k z/R_0)}{\cosh(\lambda_k H_0/R_0)} \tag{2.1}$$

is zero at the endwalls and contains only even terms of the radial coordinate power expansion. Here $J_1(x)$ is the Bessel function of the first kind and λ_k are the roots of $J_1'(x) = 0$.

The problem is considered in stream function and vorticity formulation. Let us introduce variables Ω, H and W as follows:

$$v_\phi(z,r) = \Omega(z,r)r, \quad \psi(z,r) = -0.5r^2H(z,r), \quad w(z,r) = W(z,r)r, \tag{2.2}$$

where $w(z,r)$ is the azimuthal vorticity component:

$$w(z,r) = \boldsymbol{e}_\phi \cdot (\nabla \times \boldsymbol{v}), \tag{2.3}$$

and $\psi(z,r)$ is the stream function of the axially symmetric meridional flow:

$$\boldsymbol{v} = -\nabla \times \left(\frac{\psi}{r}\boldsymbol{e}_\phi\right), \tag{2.4}$$

with $\boldsymbol{v} = v_r\boldsymbol{e}_r + v_z\boldsymbol{e}_z$. The velocities of the meridional flow $\boldsymbol{v}$ are expressed as follows:

$$v_z = H + 0.5r\frac{\partial H}{\partial r}, \quad v_r = -0.5r\frac{\partial H}{\partial z}. \tag{2.5}$$

These definitions of Ω, W and H can also be treated as an extension of the von Kármán similarity variables (see the review by Zandbergen & Dijkstra 1987) to a laterally confined flow. Using the scales ν/H_0, H_0^2/ν and H_0 or R_0 for velocity, time, and axial or radial coordinate, respectively, the Navier–Stokes equation and equation (2.3) for the functions Ω, W and H can be written

$$\frac{\partial \Omega}{\partial t} + \mathcal{N}(\Omega) - \frac{\partial H}{\partial z}\Omega = \mathcal{L}(\Omega) + Ta_m f(z,r), \tag{2.6}$$

$$\frac{\partial W}{\partial t} + \mathcal{N}(W) - \frac{\partial \Omega^2}{\partial z} = \mathcal{L}(W), \tag{2.7}$$

$$\mathcal{L}(H) + 2W = 0, \tag{2.8}$$

where

$$\mathcal{L} = \frac{1}{R^2}\frac{1}{r^3}\frac{\partial}{\partial r}r^3\frac{\partial}{\partial r} + \frac{\partial^2}{\partial z^2}, \quad \mathcal{N} = \left(H + \frac{r}{2}\frac{\partial H}{\partial r}\right)\frac{\partial}{\partial z} - \frac{r}{2}\frac{\partial H}{\partial z}\frac{\partial}{\partial r}.$$

The so-called magnetic Taylor number $Ta_m = Re_\omega Ha^2 = \omega\sigma B_0^2 H_0^4/(2\nu^2\rho)$ and the aspect ratio $R = R_0/H_0$ are the two governing parameters of the problem. The different scales for the axial and radial coordinates result in the convenient computational domain $[-1{:}1] \times [0{:}1]$. The cylinder radius was traditionally used for deriving velocity and time scales in previous investigations. Our choice of the cylinder height is motivated by the fact that only the radial part of the linear operator $\mathcal{L}$ then contains the aspect ratio in (2.6)–(2.8).

The no-slip boundary conditions for equations (2.6)–(2.8) are

$$\Omega(\pm 1, r) = \Omega(z, 1) = 0, \tag{2.9}$$

$$H(\pm 1, r) = H(z, 1) = 0, \quad \frac{\partial H}{\partial z}(\pm 1, r) = \frac{\partial H}{\partial r}(z, 1) = 0. \tag{2.10}$$

3. Numerical techniques

3.1. *Spectral approximations*

We express the steady solution of the problem (2.6)–(2.10) via base functions constructed from the orthogonal Chebyshev polynomials $T_n(x)$ to meet the boundary and symmetry conditions

$$\Omega(z,r)=\sum_{i=0}^{N_z}\sum_{j=0}^{N_r}\Omega_{ij}G_{2i}(z)G_{2j}(r),\qquad H(z,r)=\sum_{i=0}^{N_z}\sum_{j=0}^{N_r}H_{ij}H_{2i+1}(z)H_{2j}(r),\tag{3.1}$$

where $G_n(x)=T_n(x)-T_{n+2}(x)$ and

$$H_n(x)=T_n(x)-2\frac{n+2}{n+3}T_{n+2}(x)+\frac{n+1}{n+3}T_{n+4}(x)$$

satisfy $G_n(\pm1)=0$ and $H_n(\pm1)=H_n'(\pm1)=0$, respectively (cf. equation 18 in Gelfgat & Tanasawa 1994). The body force is an even function of the axial coordinate z and the boundary conditions are symmetric. Hence, the steady angular velocity distribution Ω is an even and H is an odd function of z as follows from (2.6)–(2.8). The approximation (3.1) was used to find the steady solution. Therefore the symmetry of the problem with respect to the mid-plane $z=0$ is taken into account in (3.1). Concerning the flow stability, however, the steady solution can become unstable with respect to an anti-symmetric perturbation as well:

$$\Omega'(z,r)=\sum_{i=0}^{N_z}\sum_{j=0}^{N_r}\Omega'_{ij}G_{2i+1}(z)G_{2j}(r),\qquad H'(z,r)=\sum_{i=0}^{N_z}\sum_{j=0}^{N_r}H'_{ij}H_{2i}(z)H_{2j}(r).\tag{3.2}$$

Alternatively the time-dependent solution is sought in standard Chebyshev tau form:

$$\left.\begin{aligned}\Omega(z,r,t)=\sum_{i=0}^{M_z}\sum_{j=0}^{M_r}g_{ij}(t)T_i(z)T_{2j}(r),\qquad W(z,r,t)=\sum_{i=0}^{M_z}\sum_{j=0}^{M_r}w_{ij}(t)T_i(z)T_{2j}(r),\\ H(z,r,t)=\sum_{i=0}^{M_z}\sum_{j=0}^{M_r}h_{ij}(t)T_i(z)T_{2j}(r).\end{aligned}\right\}\tag{3.3}$$

including even and odd modes of the axial coordinate expansions to allow vertical symmetry breakdown due to the instability.

The axial symmetry condition is satisfied by including only even radial coordinate modes in expansions (3.1)–(3.3). These expansions satisfy the conditions usually applied at the axis ($v_\phi=0$, $v_r=0$, $\partial v_z/\partial r=0$) as it is seen from (2.2) and (2.5). This simple approach seems not to have been widely employed and, therefore, we provide a proof. If a scalar function $F(x,y)$ can be expanded in a coordinate power series (which means that the function is infinitely differentiable) for $x^2+y^2\leqslant 1$ and satisfies the axial symmetry condition $F(x,y)=F(-x,-y)$ then each of its power expansion terms $a_{nm}x^ny^m$ must also satisfy this condition. Consequently, either $n+m$ is an even number or $a_{nm}=0$. Recalling polar coordinates $x=r\cos\phi$, $y=r\sin\phi$ it follows that the expansion of function F contains only even powers of r (J. Priede, private communication). Similarly it can be shown that an expansion of an axially symmetric vector function $\boldsymbol{f}(x,y)=(f_x,f_y)=-\boldsymbol{f}(-x,-y)$ contains only odd powers of r.

3.2. *Steady solution and linear stability*

The steady solution was found by the weighted residual procedure. We substituted (3.1) in (2.6)–(2.8) and required the residual to be orthogonal to each $T_{2i+p}(z)\,T_{2j}(r)$ for $i = 0, 1 \ldots, N_z$; $j = 0, 1 \ldots, N_r$; $p = 0$ or $p = 1$ for equations (2.6) or (2.7), (2.8), respectively. This leads to a set of nonlinear equations of the form

$$\boldsymbol{A}\dot{\boldsymbol{x}} = \boldsymbol{L}\boldsymbol{x} + \boldsymbol{N}(\boldsymbol{x}) + \boldsymbol{F}, \tag{3.4}$$

where $\boldsymbol{A}$ is the so-called mass matrix. The steady solution $\boldsymbol{x}_0$ of (3.4) was found by the Newton method through successive iterative improvements.

Taking into account the vertical symmetry of the problem (2.6)–(2.10), the dynamical equations for even and odd axial coordinate modes decouple in the vicinity of the symmetric steady state. On inverting $\boldsymbol{A}$, the dynamical system

$$\dot{\boldsymbol{u}} = \boldsymbol{J}\boldsymbol{u} \tag{3.5}$$

follows for the small perturbation $\boldsymbol{u} = \boldsymbol{x} - \boldsymbol{x}_0$ of appropriate symmetry containing even angular velocity and odd stream function modes of the axial coordinate expansion, where $\boldsymbol{J} = \boldsymbol{A}^{-1}(\boldsymbol{L} + (\partial \boldsymbol{N}/\partial \boldsymbol{x})|_{\boldsymbol{x}_0})$ is the Jacobi matrix. Similarly, the dynamical system for the opposite vertical symmetry perturbation $\boldsymbol{u}'$ (3.2) can be obtained in the form $\dot{\boldsymbol{u}}' = \boldsymbol{J}'\boldsymbol{u}'$. The sign of the real part of the dominant eigenvalue $\lambda = \lambda_r + \mathrm{i}\lambda_i$ of the matrices $\boldsymbol{J}$ and $\boldsymbol{J}'$ determines if the steady solution is linearly stable or not. The eigenvalue problem was solved using routine DGEEVX from the linear algebra package LAPACK.

3.3. *Time-dependent solution*

Alternatively, we solve the problem (2.6)–(2.10) by numerically integrating in time. The second-order implicit time discretization of (2.6) at moment t_{n+1} is written

$$\frac{3\Omega^{n+1} - 4\Omega^n + \Omega^{n-1}}{2\Delta t} = \mathscr{L}(\Omega^{n+1}) + 2q^n - q^{n-1}, \tag{3.6}$$

where q includes the body force and the convective term (Lopez & Shen 1998). This leads to a Helmholtz type equation for angular velocity at each time step. Employing the Chebyshev tau approximation (3.3), a set of linear algebraic equations follows for Ω_{ij}^{n+1} in the matrix form $\boldsymbol{L}_z\boldsymbol{\Omega} - \boldsymbol{\Omega}\boldsymbol{L}_r - 1.5/\Delta t\boldsymbol{\Omega} = \boldsymbol{Q}$, where matrices $\boldsymbol{L}_z$ and $\boldsymbol{L}_r$ stand for axial and radial discrete presentations of the diffusive operator $\mathscr{L}$, respectively. This set was solved by separating the radial dependence using the diagonalization technique and fast factorization in the axial direction (Canuto *et al.* 1988).

The absence of explicit boundary conditions for the vorticity is compensated by double conditions for the stream function (2.10). This fourth-order problem was decoupled following Auteri & Quartapelle (1999). A brief description of the procedure is given in the Appendix.

The nonlinear terms were evaluated pseudo-spectrally by projecting the solution to real space values on the Gauss–Lobato mesh by means of the fast Fourier transform. The '3/2 rule' was used to eliminate the aliasing error (Canuto *et al.* 1988).

3.4. *Numerical tests*

We tested the numerical techniques by evaluating the relative difference between numerical solutions of different spatial resolution. The steady solutions obtained by the Newton method (§ 3.2) and the steady states of the time-dependent solution (§ 3.3) were examined. The time-dependent solution was assumed steady when the relative variation of its leading decomposition modes $g_{00}(t)$, $h_{10}(t)$ was less than 10^{-9} during

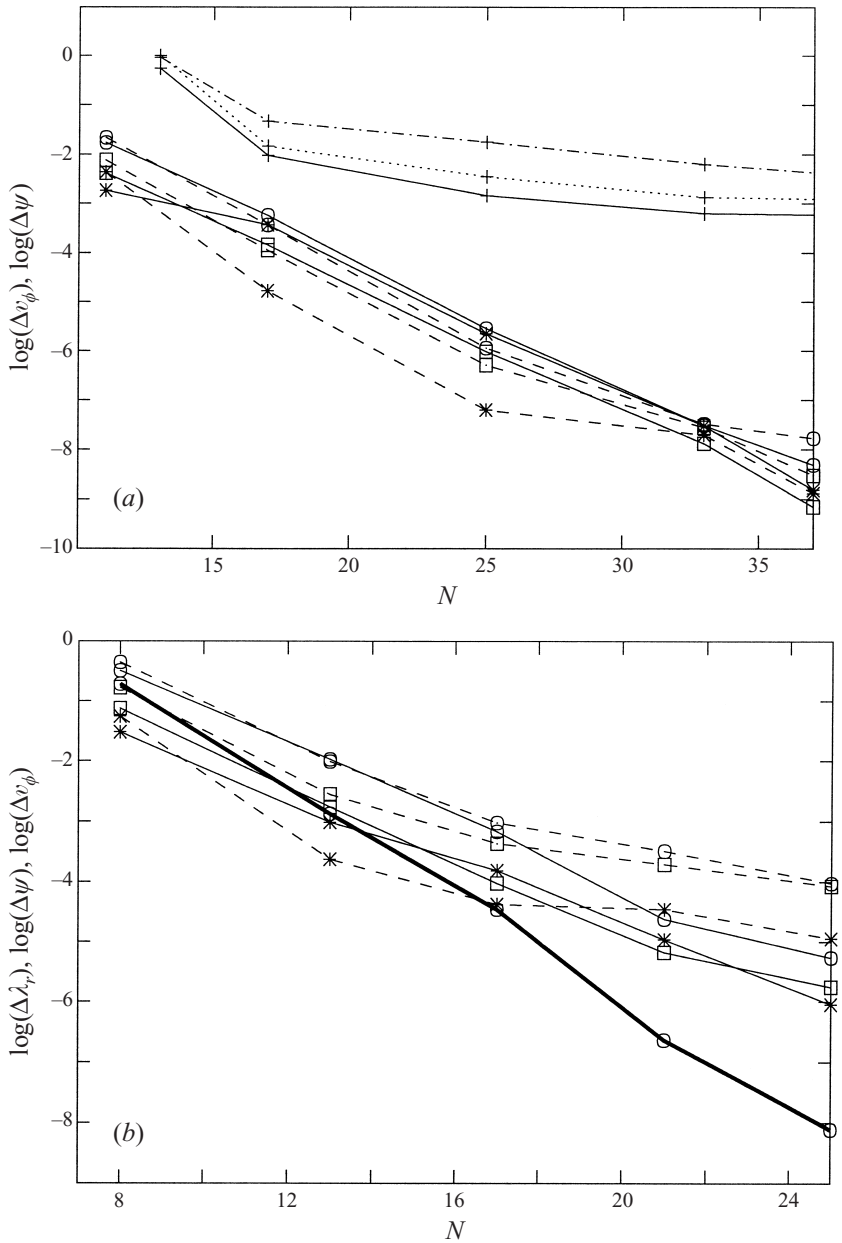

FIGURE 1. The scaled error of azimuthal velocity (solid lines), stream function (dashed lines) and the dominant eigenvalue (thick line) versus spatial resolution for (*a*) steady time-dependent solution and (*b*) direct steady solution; $R = 1$, $Ta_m = 0.4 \times 10^4$. Symbols ⊙ □ and ∗ mark the maximum absolute error, the norm of the error and the error of the maximum value, respectively; + mark results from FIDAP in terms of maximum absolute error; dash-dotted and dotted lines correspond to axial and radial velocity, respectively.

the characteristic dimensionless time $\tau_0 = \Omega_0^{-1/2}$. The steady time-dependent solution with a spatial resolution ($M_z = 108$, $M_r = 54$) was used as a reference state. We considered a test case with a moderate forcing $Ta_m = 0.4 \times 10^5$ and the aspect ratio $R = 1$. The Reynolds number of the primary rotation was $Re = \max(v_\phi(z, r)) = 391.1$

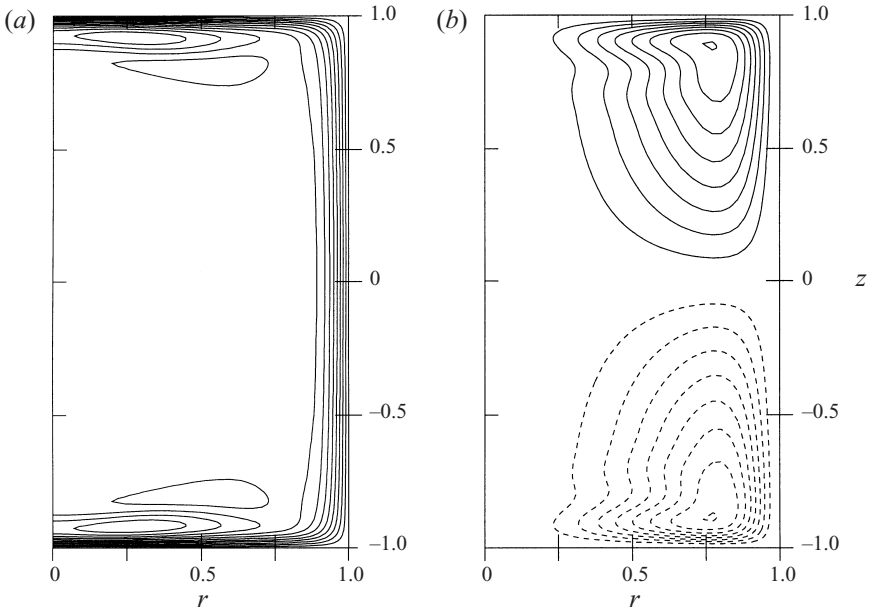

FIGURE 2. Steady solution near the linear stability threshold: (*a*) angular velocity isolines with a step 150; (*b*) streamlines of the meridional flow with step 2; $Ta_m = 1.6 \times 10^5$, $R = 1$.

and the maximum stream function value was $\psi_0 = \max(\psi(z,r)) = 8.845$, respectively. Additionally we solved the test problem by the finite element method implemented in the commercial fluid dynamics program FIDAP. Biquadratic quadrilateral elements of third-order spatial approximation were used.

Figure 1 depicts the solution convergence in terms of the maximum absolute error $\max|v_\phi(z,r) - v_\phi^{ref}(z,r)|/Re^{ref}$ or $\max|\psi(z,r) - \psi^{ref}(z,r)|/\psi_0^{ref}$, the error norm

$$\|\Delta v_\phi\| = \left(\frac{\int_V (v_\phi - v_\phi^{ref})^2 \, \mathrm{d}V}{\int_V (v_\phi^{ref})^2 \, \mathrm{d}V} \right)^{1/2} \quad \text{or} \quad \|\Delta\psi\| = \left(\frac{\int_V (\psi - \psi^{ref})^2 \, \mathrm{d}V}{\int_V (\psi^{ref})^2 \, \mathrm{d}V} \right)^{1/2}$$

and the error of the maximum value $|\max(v_\phi(z,r))/Re^{ref} - 1|$ or $|\max(\psi(z,r))/\psi_0^{ref} - 1|$ depending on the spatial resolution. Here v_ϕ^{ref} or ψ^{ref} stand for the reference distributions and Re^{ref} or ψ_0^{ref} are the corresponding maximum values. The spatial resolution was defined as the number of unknowns per variable per coordinate, that is $N = (N_z + 1) = (N_r + 1)$ for the direct steady solution and $N = (M_z/2 + 1) = (M_r + 1)$ for the steady time-dependent solution. The error of the real part of the dominant eigenvalue is depicted in figure 1(*b*) with the reference value the $N = 29$ resolution steady solution.

4. Results

4.1. *Basic steady solution*

The steady solution in the near-critical regime has an almost rigidly rotating core (figure 2) separated from the endwalls by pronounced horizontal boundary layers.

R	$N_z \times N_r$	$Ta_m^{cr} \times 10^{-5}$	λ_i^{cr}	R	$N_z \times N_r$	$Ta_m^{cr} \times 10^{-5}$	λ_i^{cr}
1	42×16	1.605	1632	0.5	56×16	4.7341	2890
	46×12	1.616	1643		60×12	4.7427	2895.5
	46×16	1.6359	1658.2		60×16	4.7433	2894.6
	46×20	1.6358	1659.0		60×20	4.7428	2894.4
	50×16	1.6361	1659.1		64×16	4.7434	2894.7

TABLE 1. The convergence of the critical parameters.

R	$Ta_m^{cr} \times 10^{-5}$	λ_i^{cr}	$\tilde{\lambda}_r$	Re^{cr}
1	1.636	1659	−26.2	1117
0.93	1.690	1681	−29.9	1068
0.85	1.842	1759	−32.4	1039
0.75	2.209	1945	−31.0	1034
0.67	2.707	2178	−24.2	1049
0.55	4.009	2711	−0.4	1085
0.5	4.743	2895	−18.6	1074
0.4	8.366	3804	−23.1	1177

TABLE 2. The critical parameters for variable aspect ratio.

These boundary layers have a self-similar spatially oscillating pattern. The corresponding model problem concerns a fluid rotating over an infinite, stationary disc (Davidson 1992). This model problem was first considered by Bödewadt (1940). A self-similar rotating boundary layer is sometimes referred to as an Ekman layer. We follow the terminology (e.g. Lingwood 1997) distinguishing different reference problems. Therefore we refer to the horizontal boundary layer as the Bödewadt layer. The basic solution is marked by a smooth side layer and one pair of meridional vortices (figure 2).

The dominant eigenvalue was evaluated for a gradually increasing magnetic Taylor number. The convergence of the dominant eigenvalue was verified at each step. The critical Taylor number Ta_m^{cr} was found as the root of $\lambda_r(Ta_m) = 0$. The number of axial decomposition modes required rapidly grew with increasing magnetic Taylor number while the necessary number of radial modes was constant $N_r = 16$. Thus, 46×16 modes were necessary to evaluate the critical parameters within 0.1% estimated accuracy for $R = 1$ (table 1). The analysis in a cylinder of doubled height $R = 0.5$ required the even higher axial resolution of $N_z = 60$ modes and the Newton algorithm did not converge for $N_z \leqslant 52$. Table 2 summarizes the linear instability results for aspect ratios $0.4 \leqslant R \leqslant 1$.

We found that the critical perturbation had symmetry of the basic solution for $R > 0.55$. The anti-symmetric perturbations first became unstable in an elongated cylinder with $R \leqslant 0.55$. The dominant eigenvalue of the linearly stable half-spectrum (i.e. that of the opposite symmetry with respect to the most unstable perturbation) is denoted by $\tilde{\lambda}_r$ in table 2. The critical perturbation for $R = 1$ and $R = 0.5$ is shown in figure 3.

4.2. *Other steady solutions*

Depending on the initial approximation several additional steady solutions can be found for certain ranges of forcing. We detected these solutions by varying the spatial

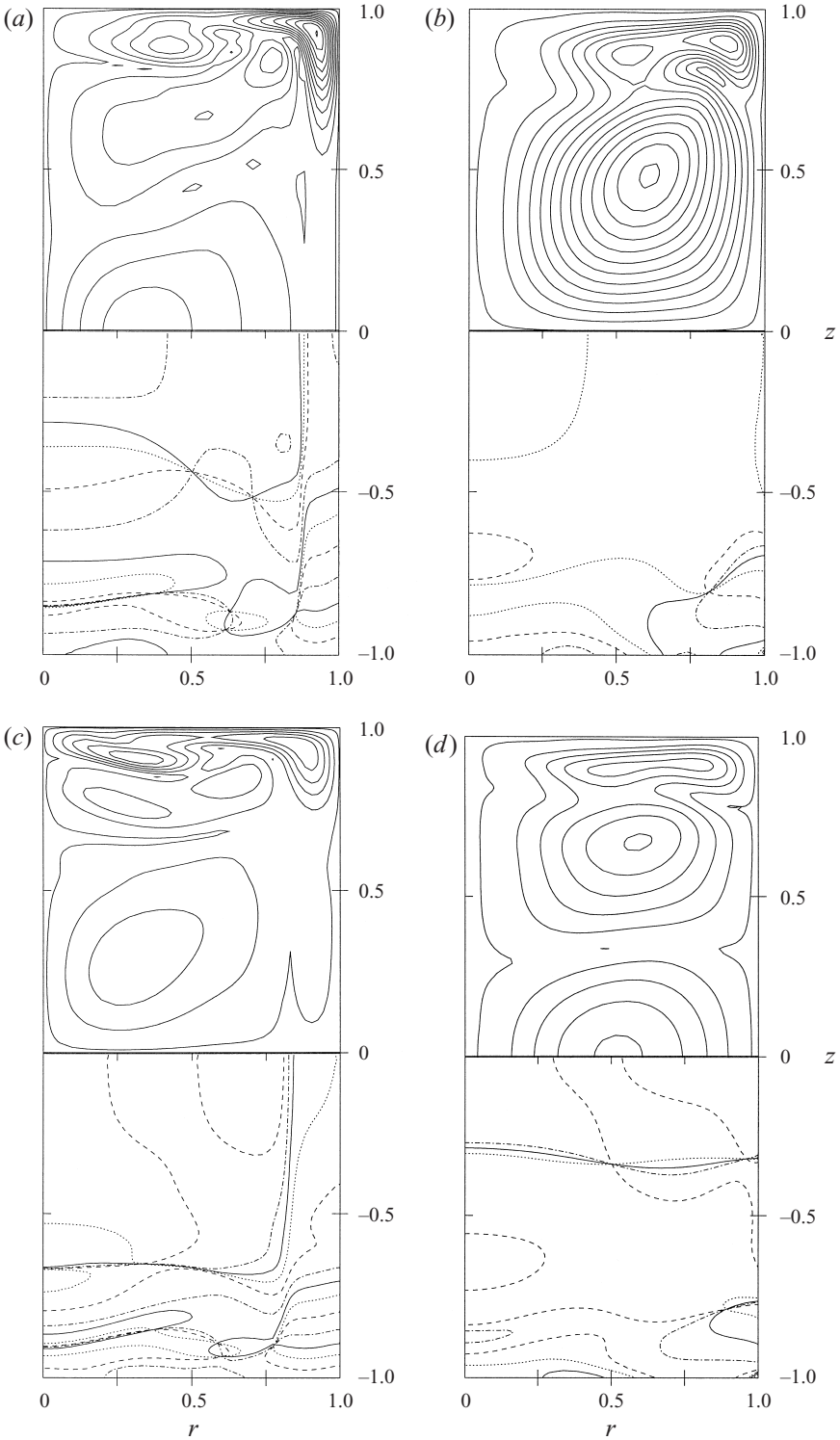

FIGURE 3. The critical perturbation of azimuthal velocity (a, c) and stream function (b, d) for $R = 1$ (a, b) and $R = 0.5$ (c, d). The upper part of each plot depicts the perturbation amplitude. Isolines are plotted with a step 0.1, 3×10^{-3}, 0.05 and 3×10^{-3} starting from 0.02, 3×10^{-4}, 0.01 and 3×10^{-4} for $(a–d)$, respectively. The lower part of each plot depicts the zero isoline of the perturbation for phase shift 0, $\pi/4$, $\pi/2$ and $3\pi/4$ with solid, dash-dotted, dashed and dotted lines, respectively.

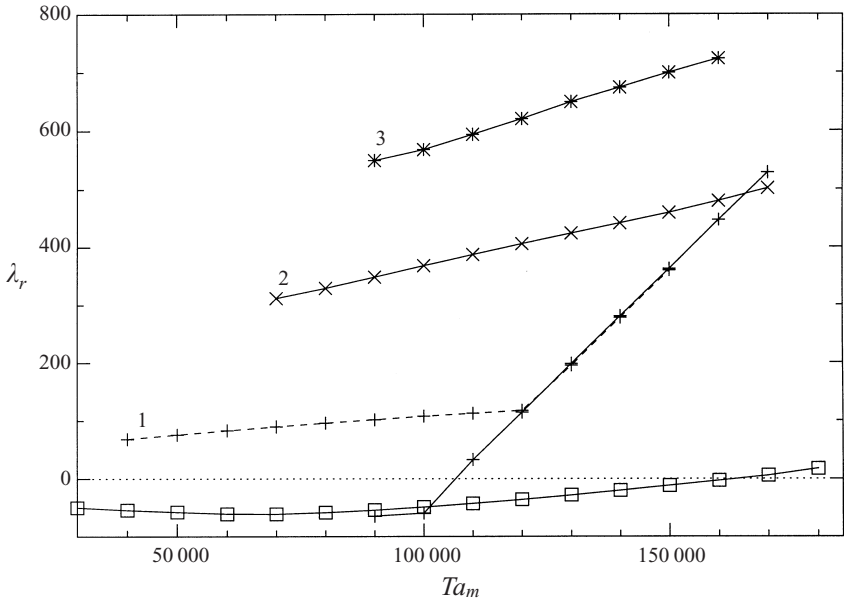

FIGURE 4. The real part of the dominant eigenvalue versus the magnetic Taylor number for various steady solution branches ($R = 1$). The basic solution is marked with □; symbols +, × and * correspond to the steady solution branches 1–3, respectively. The dashed line corresponds to the anti-symmetric spectrum of branch 1 solution.

resolution. An error in the form of the Taylor–Görtler vortices was characteristic for a low-resolution steady solution. Taking such a solution as an initial guess we detected three more branches of converging steady solutions. The convergence was verified to 0.3% accuracy in terms of the estimated error of the dominant eigenvalue. Figure 4 depicts the dependence of dominant eigenvalue of the corresponding linearized systems on the magnetic Taylor number for $R = 1$. Linear stability analysis showed that these solutions are monotonically unstable ($\lambda_i = 0$) with a high perturbation growth rate. The dominant eigenvalue of the branch 1 solution (figure 5*a–c*) belonged to the anti-symmetric part of the spectrum for $Ta_m < 1.2 \times 10^5$. This solution was linearly stable to symmetric perturbations for $Ta_m < 1.06 \times 10^5$. The dominant eigenvalues of the symmetric and anti-symmetric dynamical systems were almost identical for two other steady solution branches, 2 and 3 depicted in figure 5(*d–i*). Branch 2 was particularly close to the basic state. The distance between different steady solution branches is depicted in figure 6. The additional steady solutions 1–3 did not converge for $Ta_m < 0.38 \times 10^5$, $Ta_m < 0.68 \times 10^5$ and $Ta_m < 0.88 \times 10^5$, respectively.

4.3. *Time-dependent solutions*

The direct steady solution of (3.4) in the near-critical state required a high spatial resolution that came close to the limit of capabilities of the computers and algorithms employed. The time-dependent solution allowed much higher resolution. We compared the linear stability results in §4.1 for $R = 1$ and $R = 0.5$ to dynamical parameters of high-spatial-resolution time-dependent solutions that developed from the near-critical steady states found directly with $Ta_m \approx Ta_m^{cr}(1 \pm 0.005)$. The basic state was perturbed by an $O(10^{-4})$ relative amplitude perturbation. We integrated the solutions over some 25 oscillation periods with a temporal resolution of around 400 time steps

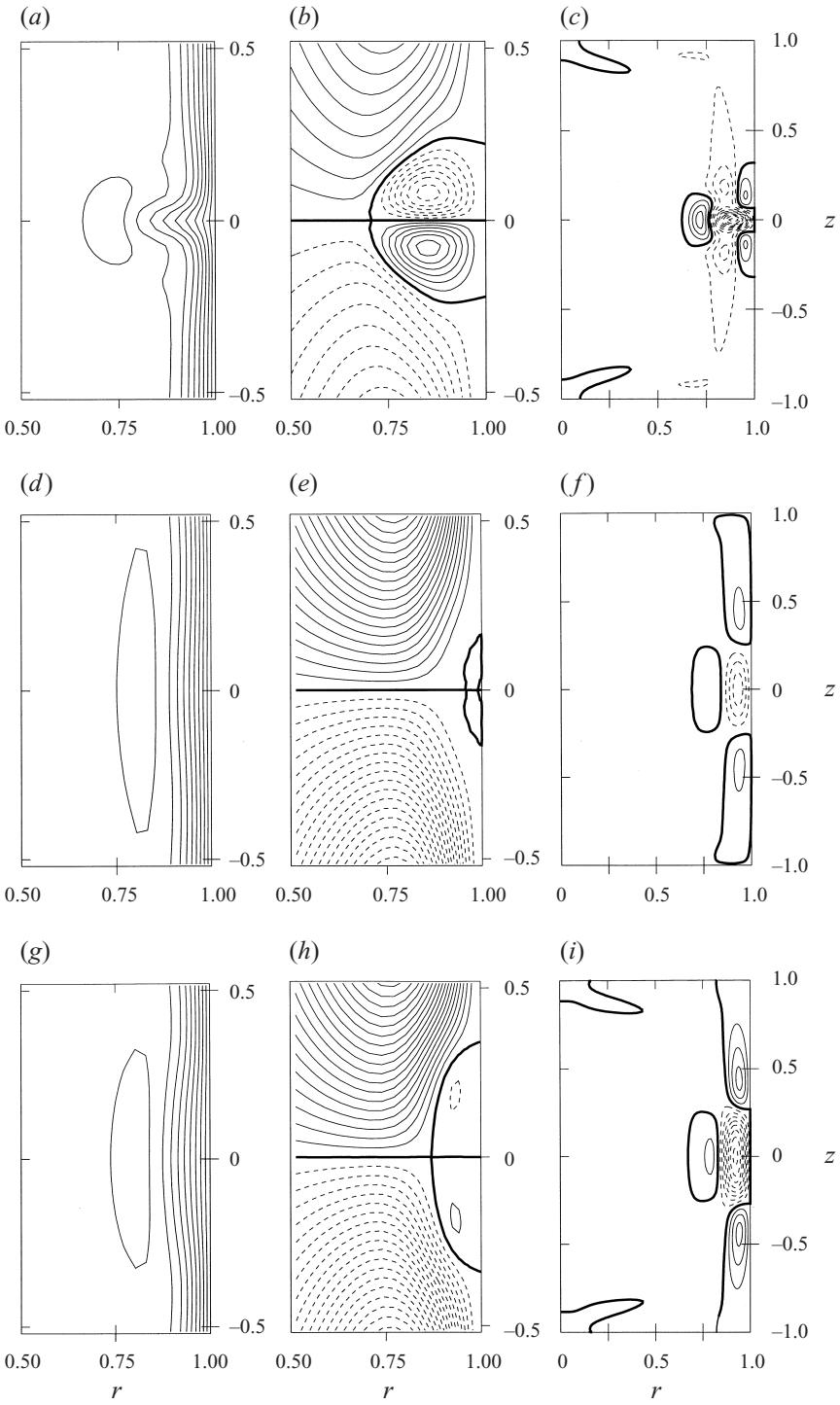

FIGURE 5. The monotonically unstable steady solution branches: (*a–c*), (*d–f*) and (*g–i*) correspond to branches 1–3, respectively; $Ta_m = 1.0 \times 10^5$, $R = 1$. Isolines of the angular velocity (a, d, g) and the stream function (b, e, h) near the neutral point at the sidewall. The isoline step is 100 and 0.5 (1.0 in plot *b*) for the angular velocity and the stream function, respectively. Plots (c, f, i) depict isolines of the difference in the angular velocity with respect to the basic state; the isoline step is 15. The negative isolines are depicted by dashed lines; the zero isoline is marked by a thick line.

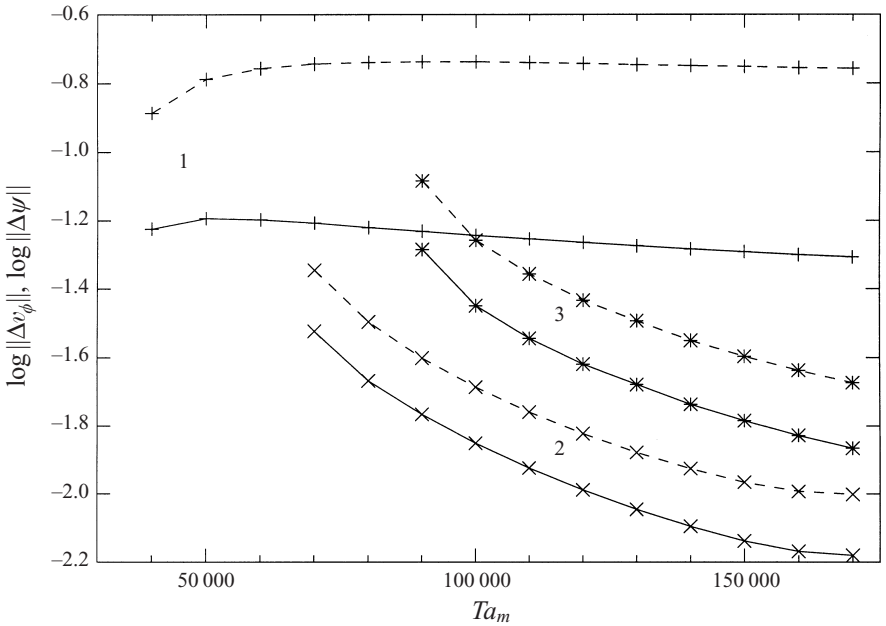

FIGURE 6. The distance $\|\Delta v_\phi\|$ (solid lines) and $\|\Delta\psi\|$ (dashed lines) from the basic steady solution versus the magnetic Taylor number ($R = 1$). Symbols $+$, $\times$ and $*$ correspond to the steady solution branches 1–3, respectively.

per period and approximated the discrete time history of the leading meridional flow mode with a function $B + A\cos(\lambda_i t + \varphi_0)e^{\lambda_r t}$ by employing the nonlinear least-squares Marquardt–Levenberg algorithm. The asymptotic standard error of both λ_i and λ_r was less than 10^{-4}. The dominant eigenvalue to be was calculated with three different spatial resolutions for $R = 1$ and $R = 0.5$ with the maximum resolution 128×48 and 144×48, respectively. The results allowed the leading eigenvalue to be evaluated within 0.1% estimated accuracy. The critical parameters found from these time-dependent solutions were $Ta_m^{cr} = 1.635 \times 10^5$, $\lambda_i^{cr} = 1659$ and $Ta_m^{cr} = 4.741 \times 10^5$, $\lambda_i^{cr} = 2894$ for $R = 1$ and $R = 0.5$, respectively. Similarly the real part of the dominant eigenvalue $\tilde{\lambda}_r$ for the stable half-spectrum was evaluated as -26.2, -0.3 and -18.4 for $R = 1$, 0.55 and 0.5, respectively.

The numerical results in § 4.2 revealed a monotonically unstable steady solution 2 close to the stable basic state. This solution can also be treated as an unstable finite-amplitude perturbation. We evaluated the dynamics of such a perturbation by taking the steady solution 2 as an initial state. Variable spatial resolution of a maximum of 144×48 modes was used. The numerical simulation showed that the steady solution 1 was established first if it was linearly stable with respect to symmetric perturbations (plateau in figure 7*a*). Then the growing unstable anti-symmetric perturbation returned the flow to the basic state. Figure 7(*a*) illustrates the history of switching between these solutions for $Ta_m = 1.0 \times 10^5$. If the steady branch 1 was also unstable to the symmetric perturbations then the basic steady solution set in after a long period of relatively big oscillations. Figure 7(*b*) illustrates this for $Ta_m = 1.2 \times 10^5$. The figure shows that the asymmetric part of the solution grew exponentially during the excited regime and the exit from this regime was marked by the maximum of flow asymmetry, reaching the characteristic scale of the flow oscillations.

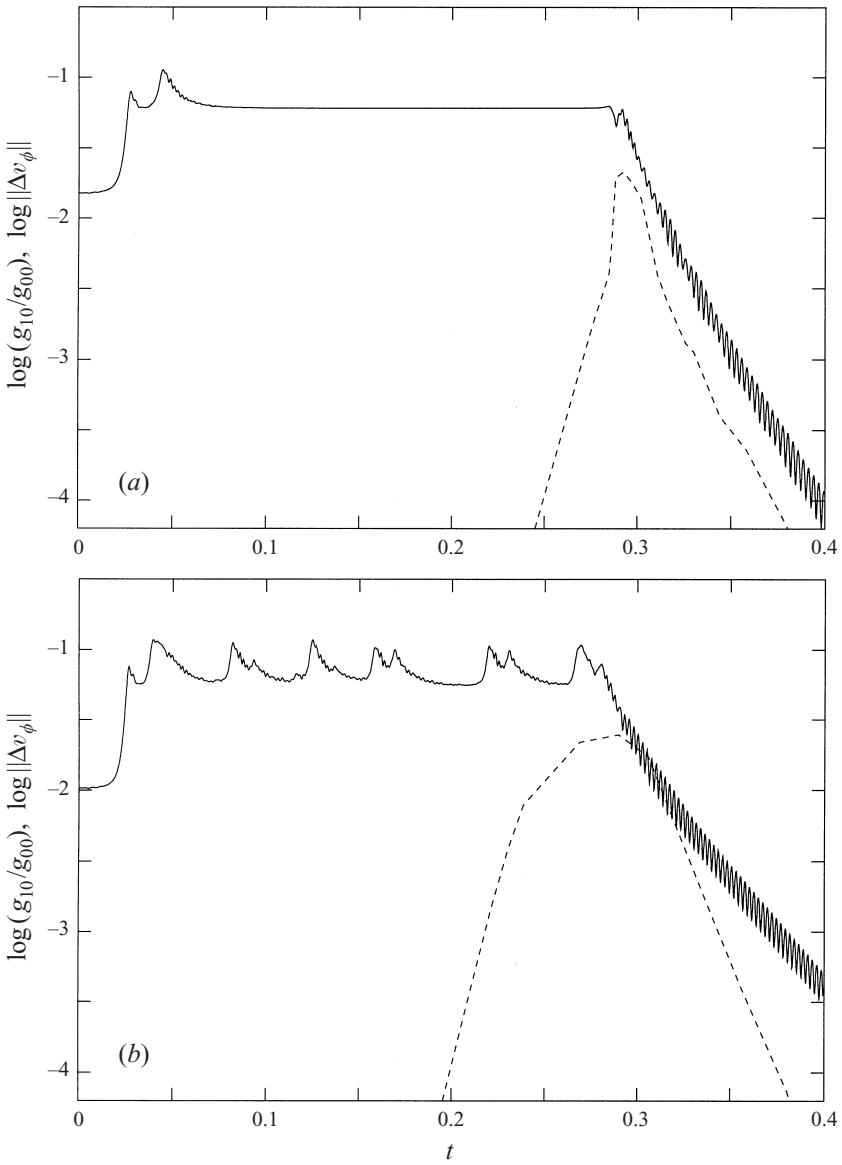

FIGURE 7. Time history of the perturbation norm developing from the unstable branch 2 (solid line): (*a*) $Ta_m = 1.0 \times 10^5$, (*b*) $Ta_m = 1.2 \times 10^5$; $R = 1$. The characteristic relative value of the leading asymmetric angular velocity mode g_{10}/g_{00} is depicted by a dashed line.

5. Discussion

Two different spectral Chebyshev approaches were employed to investigate the stability with respect to axisymmetric perturbations of a low-frequency low-induction liquid metal flow driven by a rotating magnetic field in a cylindrical cavity. The axial symmetry of the solution was enforced by including only radial coordinate modes of appropriate symmetry. This avoided the exaggerated resolution near the axis that would result from the standard approach by means of shifted polynomials $T_i(2r-1), i = 0, 1, \ldots$ (e.g. Lopez & Shen 1998). Note that the solution is marked by

a particular smoothness at the axis (figures 2, 3). Since the basic solution has vertical symmetry, the dynamical system for small perturbations separates into a symmetric (having the symmetry of the basic solution) and an anti-symmetric part. This property was used to reduce the size of the resulting eigenvalue problems. The methods were tested by comparing the steady solution from both solution methods for a moderate forcing with $Ta_m = 0.4 \times 10^5$. The steady solution was additionally compared to the results of the commercial fluid dynamics program FIDAP. The numerical tests showed a rapid convergence of the methods and an exponential convergence rate for the real part of the dominant eigenvalue up to eight significant digits (figure 1). Comparison of the results from the direct steady and time-dependent solution methods was extensively performed where possible. This particular care was undertaken because a high spatial resolution was necessary to obtain converging results in the near-critical state. The main quantitative linear stability results, i.e. the critical magnetic Taylor number and the angular oscillation frequency of the critical perturbation λ_i^{cr}, were calculated within 0.1% estimated accuracy by both methods and the results agreed at this accuracy.

The linear stability analysis showed that the basic solution becomes oscillatorily unstable at $Ta_m^{cr} = 1.635 \times 10^5$ for the aspect ratio $R = 1$ with the Reynolds number $Re^{cr} = 1117$. The angular frequency λ_i of the instability is within a factor 2 equal to the rotation frequency of the basic flow for aspect ratios between $0.4 \leqslant R \leqslant 1$ (table 2, $\Omega_0 \approx Re/R$). Hence, it remains much smaller than the frequency of the field rotation under the low-induction condition. The critical Reynolds number remains approximately constant at $Re^{cr} \approx 1100$ with 7% tolerance in the range of R considered. This qualitatively agrees with the observation by Grants (1997) and Grants & Gelfgat (1999) that the onset of the axially symmetric instability occurs at some approximately constant critical Reynolds number, calculated with the cylinder length, for aspect ratios $0.25 \leqslant R \leqslant 1.0$. This result was discussed in terms of the side layer characteristics (its thickness and the core angular velocity) by employing an analogy to the Taylor flow with a stationary outer cylinder. The present investigation revealed that the linear instability is not of the Taylor–Görtler type. Hence, the similarity to the Taylor flow does not explain the linear instability results concerning the dependence of the critical Reynolds number on the aspect ratio. However, this argument remains applicable for nonlinear instability as discussed below. The critical perturbation is localized in the core and the Bödewadt boundary layers. Its amplitude is relatively low in the side layer (except at the corner) with no Taylor vortices (figure 3). It is seen that the phase velocity of the critical perturbation has several rotation centres, marked by crossing zero isolines at different phases. Like the basic flow, the critical perturbation has a core and pronounced boundary layers at the endwalls. In the core the critical perturbation appears as an inertial wave. The critical perturbation does not have the self-similarity that is characteristic of the basic flow. These key features also appear for the critical perturbation of opposite symmetry ($R = 0.5$, figure 3c, d). We failed to obtain converging linear instability results for an elongated cylinder with the aspect ratio $R = 0.25$. This can be explained by the presence of unstable misleading steady solutions close to the basic steady state as discussed below.

We detected three additional monotonically unstable steady solution branches characterized by one more pair of meridional recirculation vortices near the neutral point at the sidewall. Evidently, such solutions can be observed only for a limited time. However, their existence has some important consequences. The presence of several steady solutions close to the basic state gives an indirect explanation for the fact that a high axial resolution is needed. The additional solutions differ from the basic

state by a relatively small correction localized in the side layer near the neutral point ($z = 0, r = 1$), where the weight of the axial approximation is minimal. We observed that solutions with poor spatial resolution preferred these 'wrong' steady states. This leads to an argument against multi-grid approaches in related problems. Such an additional steady state can also be treated as a perturbed basic solution. The solution branch 2 is particularly close to the basic state (figure 6). Hence, the corresponding finite perturbation is 'small'. The results in figure 7 show that such a purely symmetric perturbation causes a breakdown of the vertical symmetry. Thus, the flow due to a 'small' perturbation is unstable. The distance to the branch 2 solution, therefore, is an estimate of the minimum amplitude of the unstable finite perturbation. This distance is 10^{-2} or 1.5×10^{-2} in terms of the azimuthal velocity or stream function norm for $Ta_m = 1.2 \times 10^5$, $R = 1$, respectively. This estimate can be improved. For this purpose we performed several time-dependent simulations with a perturbed basic state $\boldsymbol{x}_0 + \alpha\tilde{\boldsymbol{x}}$, where $\tilde{\boldsymbol{x}}$ is some reference perturbation and α is a scale factor. The reference perturbation was taken from the time history developing from branch 2 at $t = 0.023$ (see figure 7*b*). This state is still close to the basic solution and at the same time it is marked by a rapid growth of the perturbation amplitude. Several cases with $\alpha \geqslant 1.0 \times 10^{-4}$ are shown in figure 8(*a*). It is seen that there is a small perturbation with a growing amplitude in the linearly stable regime. This is sometimes referred to as 'energetical instability'. Continuous large-amplitude oscillations with a subsequent symmetry breakdown set in for $\alpha \geqslant 0.016$ with the initial perturbation of norm $\|\Delta v_\phi\| = 2.8 \times 10^{-4}$ and $\|\Delta\psi\| = 5.3 \times 10^{-4}$. As is seen in figure 9 such an unstable finite-amplitude perturbation is of the Taylor–Görtler type. Similarly we found that there is a finite perturbation of the norm $\|\Delta v_\phi\| = 2 \times 10^{-3}$, $\|\Delta\psi\| = 5 \times 10^{-3}$ switching the basic state to the unstable branch 1 for $Ta_m = 0.7 \times 10^5$. Note that an unsteady flow example in figure 5 of Kaiser & Benz (1998) represents such an instability. The form of the reported instability corresponds to the branch 1 steady solution (cf. figure 5*a*, *b*). The unsymmetric location of the Taylor rolls is explained by the vertical symmetry breakdown. This nonlinear instability can be discussed as follows. Evidently, the side layer is prone to the Taylor–Görtler instability. The tangential jet of the basic meridional flow, however, drives away and deforms the perturbation (this jet is accelerating towards the horizontal wall) everywhere but near the neutral point ($z = 0, r = 1$). If the perturbation amplitude is sufficient, the flow is attracted by the steady solution 1 with a pair of additional vortices. The new steady state, however, is unstable and the Taylor rolls are carried towards one of the horizontal boundary layers and disappear. Meanwhile, a new pair is born at the neutral point due to a small finite perturbation. Richardsons' analysis for an infinite cylinder reveals a linear Taylor–Görtler type instability. Hence, the minimum amplitude for this type of instability tends to zero as the length of a finite cylinder increases. This agrees qualitatively with the numerical time-dependent solution showing an unstable finite size perturbation of amplitude $\|\Delta v_\phi\| = 4 \times 10^{-7}$, $\|\Delta\psi\| = 10^{-6}$ in the linearly stable regime for $R = 0.25$ (figure 8*b*). This indirectly explains why the linear stability analysis failed to produce converging results for this aspect ratio.

Under laboratory conditions the geometrical imperfections and vibrations introduce a persistent source of finite-amplitude perturbations. Similarly the approximation errors introduce a persistent source of finite perturbations in the numerical simulation. To obtain an alternative estimate of the unstable perturbation amplitude we evaluated the norm of the steady solution error with decreasing spatial resolution for $Ta_m = 1.2 \times 10^5$, $R = 1$. We found that the steady solution is still available with the error norm $\|\Delta v_\phi\| = 2.5 \times 10^{-3}$, $\|\Delta\psi\| = 5 \times 10^{-3}$. A solution with a lower resolution

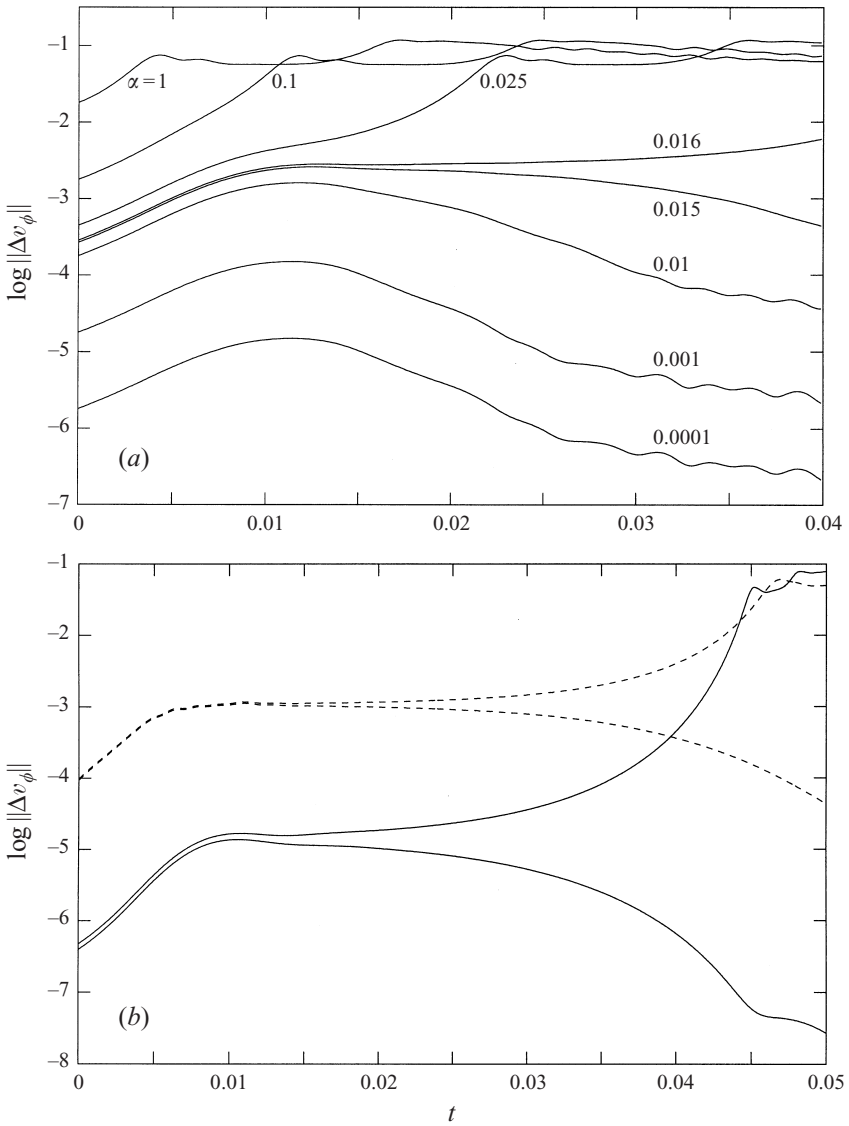

FIGURE 8. Time histories of reference perturbations of different initial size $\|\Delta v_\phi\|$: (*a*) $Ta_m = 1.2 \times 10^5$, $R = 1$; (*b*) $Ta_m = 3.6 \times 10^5$, $R = 0.5$ dashed lines and $Ta_m = 2.4 \times 10^6$, $R = 0.25$ solid lines.

and a bigger error produced an unsteady flow with the characteristic Taylor–Görtler vortices. The current investigation shows that this instability is expected to dominate in systems of practical relevance. For example, the thickness of the crucible wall for a 2 in. gallium arsenide growth is given as (0.9 ± 0.4) mm, hence the radius is constant to a 0.4% accuracy. At the same time, there is a finite size unstable perturbation of characteristic amplitude 5×10^{-4} for $Ta_m = 0.73 Ta_m^{cr}$, which means instability can appear in the linearly stable regime due to small geometrical imperfections of the crucible.

The high sensitivity of the basic flow to the finite-amplitude Taylor–Görtler vortices may indirectly explain the big differences in the previous numerical results from the

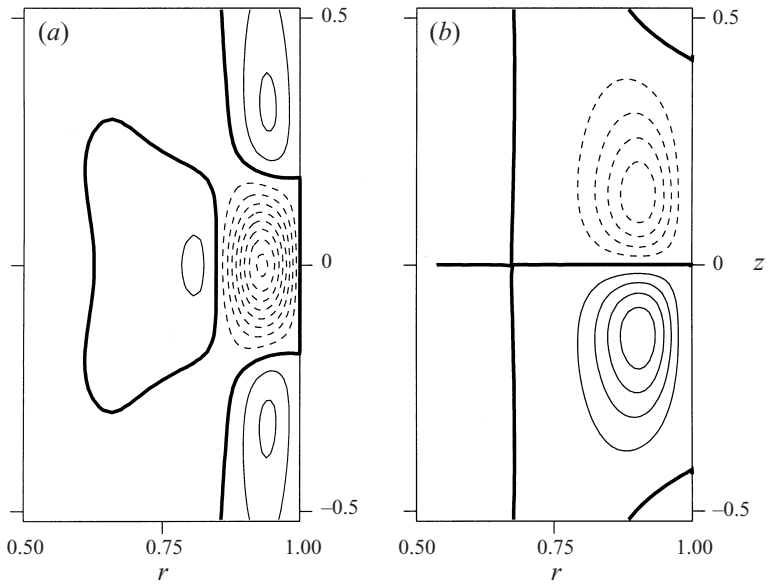

FIGURE 9. Unstable finite size reference perturbation: $Ta_m^{cr} = 1.2 \times 10^5$, $R = 1$. The perturbation norm is $\|\Delta v_\phi\| = 2.8 \times 10^{-4}$, $\|\Delta\psi\| = 5.3 \times 10^{-4}$ ($\alpha = 0.016$, see also figure 8*a*). Isolines of (*a*) the angular velocity with a step 0.2 and (*b*) the stream function with a step 0.005.

Contribution	Finite differences or control volumes	Finite elements
Barz *et al.* (1997)	2.8	
Gelfgat *et al.* (1991)	1.6†	
Grants (1997)	2.0	0.52
Kaiser & Benz (1998)		0.545
Marty *et al.* (1999)	1.75	
Mößner & Gerbeth (1999)		2.0

TABLE 3. Comparison of the critical magnetic Taylor number $Ta_m^{cr} \times 10^{-5}$ for aspect ratio $R = 1.0$ by different authors. †Calculated for a free top surface.

time integration of the Navier–Stokes equation. It is seen in table 3 that the finite difference or control volume methods produce critical values closer to the linear instability limit while the weighted approximation finite element methods yield critical values closer to the limit of global stability Ta^G that is shown to be $Ta_m^G < 0.7 \times 10^5$ for $R = 1$. Results by Mößner & Gerbeth (1999) contradict this division since the numerical techniques employed addressed the question of the convergence of the steady solution rather than its stability.

The Bödewadt layers at the endwalls are linearly unstable with respect to three-dimensional perturbations in the form of spiral waves. This type of instability was examined experimentally by Savaş (1987) and theoretically by Lingwood (1997), reporting the critical local Reynolds number $Re_l^{cr} \approx 25$ and $Re_l^{cr} = 21.6$, respectively. The local Reynolds number is defined as $Re_l^{cr} = (v_\infty l)/\nu$ where v_∞ is azimuthal velocity in the core and $l = (\nu/\Omega_0)^{1/2}$ is the characteristic boundary layer thickness. The critical Reynolds number with respect to axially symmetric perturbations is $Re^{cr} = 1117$ with

$\Omega_0 \approx 1350$ for $R = 1.0$. The corresponding maximum local Reynolds number is estimated as $Re_l = Re\,\Omega_0^{-1/2} \approx 30$, which exceeds the spiral instability threshold. Note that the instability threshold of the self-similar Bödewadt solution is expected to underestimate the critical value for the actual horizontal layer at $r > 0.6$. As reported by Lingwood (1997) the decreasingly inflectional nature of the rotating layer is accompanied by an increasingly stable flow. For example, the critical local Reynolds number 507.4 is reported for the monotonic Kármán layer near a disc rotating below a fluid at rest. The horizontal boundary layer completely loses its characteristic spatially oscillating shape at the radial coordinate $r \approx 0.85$ (see figure 2) where the core azimuthal velocity reaches its maximum. If the radial coordinate $r = 0.6$ is taken as an approximate limit where stability considerations of the Bödewadt solution are still applicable to the horizontal layer, then the local Reynolds number here is $Re_l = 21$ for $Ta_m = Ta_m^{cr}$. Hence, the aspect ratio $R = 1$ can be concluded to be an estimate of the limit at which the axisymmetric instability still dominates over the spiral instability of the horizontal layers.

The sensitivity of the flow suggests that the nonlinear instability originates from the unsymmetric rotational oscillating part of the driving force. Under the $u'/u \ll 1$ condition the induced oscillating flow $\boldsymbol{u}'$ decouples from the basic flow. The oscillating flow is described by linear equations that are solved analytically (Martin Witkowski & Walker 1999). The perturbation appears as the $\overline{(\boldsymbol{v}\cdot\nabla)\boldsymbol{u}'} + \overline{(\boldsymbol{u}'\cdot\nabla)\boldsymbol{v}}$ term in the Navier–Stokes equation, where the bar denotes averaging over the period of the electromagnetic force oscillations. Here we assume that the frequency of any possible instability remains much lower than the frequency of the field rotation. If so, the effect can be considered in an axisymmetric approximation as a small linear correction. The form of such a perturbation seems not to correspond to the Taylor rolls that probably are the most unstable finite axisymmetric perturbation. Instead, the stability analysis of a small perturbation due to a wavy sidewall promises more interesting results.

The present analysis does not consider three-dimensional perturbations. The question on the transition from axisymmetric linear instability in an infinite cylinder to the spiral instability of a horizontal layer remains open. Some other three-dimensional instability in between cannot be excluded.

The estimate of the unstable finite perturbation indicates that a very low level of imperfections and perturbations would be necessary to experimentally observe the linear instability onset. This particularly restricts the use of probe methods for liquid metal flow measurements in such an experiment. This estimate also suggests that the instability due to finite-amplitude Taylor–Görtler rolls is expected to dominate in practical applications. The uncertainty in real finite perturbations, therefore, hints that the stability limit in a specific practical system can be reasonably determined only experimentally in the system itself.

6. Conclusions

The axisymmetric liquid metal flow driven by a low-frequency low-amplitude rotating magnetic field in a cylinder of height equal to its diameter becomes oscillatorily unstable to axisymmetric perturbations at the magnetic Taylor number $Ta_m^{cr} = 1.635 \times 10^5$ with the angular frequency of oscillations $\lambda_i^{cr} = 1659$. The critical Reynolds number is to 7% tolerance constant, $Re^{cr} \approx 1100$, for aspect ratios $0.4 \leqslant R \leqslant 1$. The critical perturbation does not represent the Taylor–Görtler vortices reported in previous numerical investigations. There are several additional unstable steady solutions in the linearly stable regime of the basic flow. The latter is

attracted by such an unstable solution in the case of a small perturbation in the form of Taylor–Görtler vortices. The minimum relative amplitude of the unstable perturbation is estimated as 5×10^{-4} ($R = 1$, $Ta_m = 0.73 Ta_m^{cr}$) and decreases as the relative height of the cylinder increases. The results obtained explain contradictions in previous numerical investigations and give a minimum accuracy estimate for further theoretical or experimental studies.

The authors appreciate productive discussions with J. Priede and helpful hints by anonymous reviewers. Financial support from Saxonian Ministry of Science and Art under grant SMWK/4-7533-70-844-98/3 and Deutsche Forschungsgemeinschaft under INK 18/B1-1 is gratefully acknowledged.

Appendix. Spectral approximation of vorticity boundary conditions

There are no physical boundary conditions for the vorticity. This lack is compensated by two boundary conditions for the function H. We decoupled this fourth-order problem following Auteri & Quartapelle (1999). The vorticity at the time step t_{n+1} should satisfy a Helmholtz equation, of the form (3.6). Initially, we solved for the approximate vorticity $\tilde{W}^{n+1}$ with some approximate boundary conditions. Then, the approximate stream function $\tilde{H}^{n+1}$ with homogeneous Dirichlet boundary conditions was evaluated solving the Poisson equation (2.8) in the same way as the Helmholtz equation (3.6) was solved. This $\tilde{H}^{n+1}$, of course, does not necessarily satisfy the Neumann conditions. Thus, the task consists in finding a vorticity boundary condition correction $\hat{W}^{n+1}$ satisfying a homogeneous Helmholtz type equation and such that the corresponding $\hat{H}^{n+1}$ adjusts the Neumann condition:

$$\left.\frac{\partial \hat{H}^{n+1}}{\partial n}\right|_{\mathscr{D}} = -\left.\frac{\partial \tilde{H}^{n+1}}{\partial n}\right|_{\mathscr{D}}. \tag{A 1}$$

Here $\partial/\partial n$ denotes the derivative in the direction of the external normal and $\mathscr{D}$ stands for the domain edge. The 'corresponding' $\hat{H}^{n+1}$ means a solution of (2.8) with zero Dirichlet conditions:

$$\mathscr{L}(\hat{H}^{n+1}) = -2\hat{W}^{n+1}, \quad \hat{H}^{n+1}|_{\mathscr{D}} = 0.$$

Then the corrected solution is $W^{n+1} = \tilde{W}^{n+1} + \hat{W}^{n+1}$ and $H^{n+1} = \tilde{H}^{n+1} + \hat{H}^{n+1}$. The correction $\hat{W}^{n+1}$ is the solution of the homogeneous Helmholtz equation. Therefore it is completely determined by its trace, i.e. $M_z + M_r$ modes of the boundary conditions. It takes two steps to find $\hat{W}^{n+1}$. The preprocessing step includes solution of a homogeneous Helmholtz equation for each unitary vector of the $\hat{W}$ basis. Then the normal derivatives of the corresponding $\hat{H}$ fills matrix $\boldsymbol{A}$ in

$$\hat{\boldsymbol{h}}_n = \boldsymbol{A}\hat{\boldsymbol{w}}. \tag{A 2}$$

Here $\hat{\boldsymbol{h}}_n$ stands for the normal derivatives of the stream function correction $\hat{H}$. Once the matrix $\boldsymbol{A}$ is evaluated, it can be used at each time step to enforce (A 1) with the vorticity boundary condition correction

$$\hat{\boldsymbol{w}} = -\boldsymbol{A}^{-1}\tilde{\boldsymbol{h}}_n. \tag{A 3}$$

REFERENCES

Auteri, F. & Quartapelle, L. 1999 Galerkin spectral method for the vorticity and stream function equations. *J. Comput. Phys.* **149**, 306–332.

Barz, R. U., Gerbeth, G., Wunderwald, U., Buhrig, E. & Gelfgat, Yu. M. 1997 Modelling of the isothermal melt flow due to rotating magnetic fields in crystal growth. *J. Cryst. Growth* **180**, 410–421.

Bödewadt, U. T. 1940 Die Drehströmung über festem Grund. *Z. Angew. Math. Mech.* **20**, 241–253.

Canuto, C., Hussaini, M. Y., Quarteroni, A. & Zang, T. A. 1988 *Spectral Methods in Fluid Dynamics*. Springer.

Davidson, P. A. 1992 Swirling flow in an axisymmetric cavity of arbitrary profile, driven by a rotating magnetic field. *J. Fluid Mech.* **245**, 669–699.

Davidson, P. A. & Hunt, J. C. R. 1987 Swirling recirculating flow in a liquid–metal column generated by a rotating magnetic field. *J. Fluid Mech.* **185**, 67–106.

Gelfgat, Yu. M., Mozgirs, D., Priede, J. & Sorkin, M. Z. 1992 On the possibility of heat and mass transfer and interface shape control by electromagnetic effect on melt during unidirectional solidification. In *Hydrodynamics and Heat/Mass Transfer in Microgravity*, pp. 429–434. Gordon and Breach.

Gelfgat, Yu. M., Priede, J. & Sorkin, M. Z. 1991 Numerical simulation of MHD flow induced by rotating magnetic field in cylindrical container of finite length. In *Proc. Intl Conf. on Energy Transfer in MHD Flows*, pp. 181–186.

Gelfgat, A. Yu. & Tanasawa, I. 1994 Numerical analysis of oscillatory instability of buoyancy convection with the Galerkin spectral method. *Numer. Heat Transfer* A, **25**, 627–648.

Gorbachev, L. P., Nikitin, N. V. & Ustinov A. L. 1974 Magnetohydrodynamic rotation of an electrically conductive liquid in a cylindrical vessel of finite dimensions. *Magnitnaya Gidrodinamika* **10**, 406–414.

Grants, I. 1997 Influence of steady magnetic field and imposed rotation of the vessel on stability of magnetically driven flow. In *Proc. Third Intl Conf. on Transfer Phenomena in Magnetohydrodynamic and Electroconducting Flows*, vol. 2, pp. 409–414.

Grants, I. & Gelfgat, Y. M. 1999 Taylor–Görtler instability of a liquid metal flow in a rotating magnetic field. *Magnitnaya Gidrodinamika* **35**, 147–154.

Hurle, D. T. J. (Ed.) 1994 *Handbook of Crystal Growth*, vol. 2. Elsevier.

Kaiser, T. & Benz, K. 1998 Taylor vortex instabilities induced by a rotating magnetic field: A numerical approach. *Phys. Fluids* **10**, 1104–1110.

Lingwood, R. J. 1997 Absolute instability of the Ekman layer and related rotating flows. *J. Fluid Mech.* **331**, 405–428.

Lopez, J. M. & Shen, J. 1998 An efficient spectral-projection method for the Navier–Stokes equations in cylindrical geometries. I. Axisymmetric cases. *J. Comput. Phys.* **139**, 308–326.

Martin Witkowski, L. & Walker, J. S. 1999 Nonaxisimmetric flow in a finite-length cylinder with a rotating magnetic field *Phys. Fluids* **11**, 1821–1826.

Marty, Ph., Martin Witkowski, L., Trombetta, P. & Tomasino, T. 1999 On the stability of rotating MHD flows. In *Transfer Phenomena in Magnetohydrodynamic and Electroconducting Flows* (ed. A. Alemany, Ph. Marty & J. P. Thibault) pp. 327–343.

Moffatt, H. K. 1965 On fluid flow induced by a rotating magnetic field *J. Fluid Mech.*, **22**, 521–528.

Mössner, R. & Gerbeth, G. 1999 Buoyant melt flows under the influence of steady and rotating magnetic fields. *J. Crys. Growth* **197**, 341–354.

Priede, J. 1993 Theoretical study of a flow in an axisymmetric cavity of finite length, driven by a rotating magnetic field. PhD thesis, Institute of Physics, Latvian Academy of Sciences.

Richardson, A. T. 1974 On the stability of a magnetically driven rotating fluid flow. *J. Fluid Mech.* **63**, 593–605.

Savaş, Ö. 1987 Stability of Bödewadt flow. *J. Fluid Mech.* **183**, 77–94.

Zandbergen, P. J. & Dijkstra, D. 1987 Von Kármán swirling flows. *Ann. Rev. Fluid Mech.* **19**, 465–491.